# Microstructural analysis of W irradiated at different temperatures

M. Klimenkov[1*], M. Dürrschnabel[1], U. Jäntsch[1], P. Lied[1], M. Rieth[1], H.C. Schneider[2], D. Terentyev[3], W. Van Renterghem[3]

[1]Karlsruhe Institute of Technology (KIT), Institute for Applied Materials- Applied Materials Physics, 76021 Karlsruhe, Germany

[2]Karlsruhe Institute of Technology (KIT), Institute for Applied Materials - Mechanics of Materials and Interfaces, 76021 Karlsruhe, Germany

[3]SCK CEN, Nuclear Materials Science Institute, Boeretang 200, 2400 Mol, Belgium

* corresponding author, contact: michael.klimenkov@kit.edu

## Abstract

Pure W was neutron irradiated at 600 °C, 900 °C, 1000 °C, 1100 °C, and 1200 °C with a dose of ~1 dpa, and its microstructure was subsequently analyzed using transmission electron microscopy (TEM). Three types of defects were observed and analyzed in detail: (i) voids, (ii) dislocation loops with a diameter of up to 20 nm and (iii) precipitates containing W-Re-Os. The size and spatial distribution of the voids as well as the nature of the dislocation loops were studied in-depth. TEM analysis proved the formation of both ½<111> and <100> loops. In addition, local chemical and structural analysis revealed the formation of χ-type precipitates, which are attached to voids at 1100 °C. It was also found that voids, loops and precipitates are surrounded by a solid solution cloud enriched with Re and Os. The use of highly sensitive nanoscale chemical analysis allows the identification of differences in Re/Os segregation at and in the vicinity of the three defect types. A precise analysis of the chemical composition of the precipitates and clouds around the voids was achieved by a special preparation of their replicates.

**Key words**: tungsten, neutron irradiation, microstructure, transmutation, voids, radiation induced defects

# 1. Introduction

Tungsten (W) is the most cited material candidate for high-temperature vacuum or inert gas applications in energy technology. Due to its favorable properties, such as a very high melting point in combination with high creep and sputter resistance, a low coefficient of thermal expansion and a rather high thermal conductivity, it theoretically allows the raise of process temperatures into previously unknown temperature ranges. Besides renewable power generation methods, such as for example concentrated solar power, future fusion reactors will greatly benefit in particular by using W in plasma-facing structural parts. In the latter case, the material has to withstand very high operation temperatures as well as it has to tolerate a significant amount of radiation-induced damage [1–3]. A detailed experimental understanding of neutron damage processes at the nanoscale, which is currently limited, is of utmost importance for material qualification.

Extensive microstructural characterizations of W have already been carried out to understand the microstructural response to neutron irradiation [3–8]. However, the covered irradiation doses and temperature ranges in these investigations are limited. Increasing both parameters to the conditions expected in a future fusion reactor will address the unsolved problems regarding the microstructure.

Basically, there are three mechanisms that may degrade the beneficial material properties of W during neutron irradiation: (1) The formation of lattice defects such as Frenkel pairs, interstitial and vacancy clusters as well as dislocation loops, which cause the typical irradiation hardening and embrittlement. (2) The formation of voids leads to swelling. Both swelling and embrittlement by radiation hardening restrict the component lifetime beyond certain design limits [9]. (3) Neutron transmutation processes lead to the formation of rhenium- (Re) or osmium- (Os) rich phases. This effect can induce further significant embrittlement of W materials.

An additional issue arises with the experimental determination of the occurrence and dynamics of irradiation defects in material test reactors, which are fission-based. Such defects do not only depend on the neutron flux and temperature, but also on the specific neutron spectrum that determines the transmutation rates of the various isotopes. Therefore, the reactor type, the design of the testing rigs, and the exact irradiation position within the reactor are highly relevant for the interpretation of the experimental results. As a consequence, the outcome of an irradiation campaign has to be considered as a unique result, which adds to a more complete systematization, understanding and thereby prediction of neutron radiation damage.

Temperature significantly affects defect migration and consequently the evolution of radiation-induced defects in W. Examination of W irradiated over a wide range of temperatures, as it was done in the present study, allows the evaluation of material applications under various working conditions. Therefore, in this work we focus not only on the comprehensive characterization of radiation-induced loops and voids but also on the Re- and Os-precipitation on radiation induced defects as well as on the formation of Re- and Os-precipitates themselves. Moreover, as far as possible we examine and analyze the influence of grain boundaries on formation of defects formation and Os and Re segregation.

## 2. Experimental

The investigated polycrystalline W is of technical purity, i.e., 99.97 wt%. It is the so-called baseline armor material for ITER and DEMO applications and was supplied in the form of a bar with dimensions 36×36×480 $mm^3$, manufactured and stress relieved by PLANSEE SE, Austria. The manufacturer provides the upper limit concentration for impurities of C, O, N, Fe, Ni, Si, with typical values in parentheses as 30 (6), 20 (2), 5 (1), 30 (8), 20 (2) and 20 (1) µg/g. This material has already been extensively studied in terms of mechanical properties, interaction with plasma and high heat flux loadings (see e.g. [10–12]). The reference microstructure of this material is characterized in [11].

The samples were irradiated by neutrons up to a damage dose between about 0.86 and 0.92 dpa at five temperatures 600 °C, 900 °C, 1000 °C, 1100 °C and 1200 °C at the Belgian Nuclear Research Center SCK-CEN, Mol (Belgium) (Table 1). The irradiation was performed directly inside a channel within a fuel element. The irradiation rig was made of a tick-wall pressurized tube, which had a dual function: pressure-barrier and shielding to screen thermal neutrons. The temperature on the samples was actively controlled by the adjustment of helium flow inside the rig. The Helium environment also prevented oxidation under high temperature exposure. The total irradiation time was 143-186 days (depending on the specific capsule) and the neutron flux was (1.9-2.6)×$10^{14}$ (E > 0.1 MeV), (0.89-1.2)×$10^{14}$ (E > 1 MeV) n/$cm^2$/s. The neutron flux was calculated using the MCNPX 2.7.0 code as well as confirmed by dosimetry measurements using Fe and Nb dosimeters, applied to measure the fast neutron fluence (> 1 MeV) [13]. The dpa cross sections for W have been prepared from the JENDL4 file (MT444) for a threshold displacement energy of 55 eV.

Calculations of the transmutation inventory was performed using the ALEPH code [14,15] by assessing the propagation of the neutron spectrum from the fuel channel through to the stainless steel wall and then inside the sample. The transmutation induced content of Re and Os was determined to be ~2 at% and 0.2 at%, respectively. Without the stainless-steel shielding, the rhenium transmutation was estimated to be ~4 at% per dpa unit if the same irradiation positions would be have been used. However due to uncertain position of lamella in the sample the content of transmutation elements could show some variation due to the self-shielding effect (i.e. absorption of thermal neutrons by outer part of the thick tungsten sample, which leads to a difference in the Re/Os amount in the middle and at the edge of the sample). More details about the irradiation device and results on mechanical tests could be found in Refs. [16,17].

Table 1: Irradiation parameters of W used for this study.

| **Temperature** | **600 °C** | **900 °C** | **1000 °C** | **1100 °C** | **1200 °C** |
|---|---|---|---|---|---|
| **Dose /dpa** | 0.922 | 0.902 | 0.925 | 0.922 | 0.862 |

Since the material is radioactive, it was advantageous to use a focused ion beam instrument (FIB, FEI Scios) for sample preparation in order to (i) limit radiation exposure and (ii) perform sample preparation in a pre-defined area. Preparation using the FIB technique was performed in the Fusion Materials Laboratory (FML) at KIT. The thin lamellae were attached to a

molybdenum grid. After preparation and initial examination, the lamellae were flash polished in 1% NaOH water solution using method described in the ref. [18].

The microstructural examination was carried out using a Thermofisher Talos F200X transmission electron microscope (TEM) equipped with four energy-dispersive X-ray (EDX) detectors. The EDX detector resolution is specified by the manufacturer as ≤136 eV at Mn-$K_\alpha$. At the W-$L_\alpha$ (E = 8.396 keV) the energy resolution has a value of about 150-160 eV, which is sufficient to separate the W-$L_\alpha$, Re-$L_\alpha$ and Os-$L_\alpha$ X-ray lines. The TEM images and selected area diffraction pattern (SAED) were acquired by using a Thermofisher Ceta 16M CCD camera. The STEM-EDX maps were acquired in the Velox software using 512 x 512 pixels and a spectral dispersion of 5 eV.

Table 2: Summary of crystal structures of W-Re binary compounds used for structural identification.

| Phase | ICSD No. | Space group | Lattice |
|---|---|---|---|
| **W** | 43421 | Im-3m | cubic, bcc, a = 3.17 Å |
| **σ-$WRe_2$** | 150547 | P42/mnm | tetragonal, a = b = 9.43 Å, c = 4.99 Å |
| **χ-$WRe_3$** | 650196 | I-43m | cubic, a = 9.60 Å |

ImageJ soft was used for statistical analysis of TEM images [19]. The FFT images with structural reflections obtained from high-resolution phase contrast images were fitted with the JEMS software package [20]. The crystallographic structures of the W-Re individual phases that were used as input are summarized in Table 2.

# 3. Results

The detailed TEM analyses revealed the occurrence of three types of irradiation defects: (i) voids, (ii) dislocation loops with b½<111> and <100> Burgers vectors and (iii) W-Re-Os containing precipitates, which were identified to be χ-phase. A detailed TEM characterization of all three defect types, formed at different temperatures, is presented in the next subsections. From the previous studies of neutron irradiated W and beryllium it is well known [6,21] that the accumulation of irradiation defects near a grain boundary (GB) differs from those in the grain interior, i.e., a so-called denuded zones form close to grain boundaries, which is depleted by or even completely free of voids.

## 3.1. Distribution of voids

Figure 1 shows the void microstructure formed in W irradiated at five different temperatures. All micrographs were taken with the same magnification. The lamellae were cleaned by flash polishing, removing all surface layers that were damaged by the FIB preparation. Unfortunately, flash polishing can lead to uneven etching of the surfaces. Therefore, thickness

variations are visible in some images. The images clearly show that the voids within the grains have a homogeneous spatial distribution.

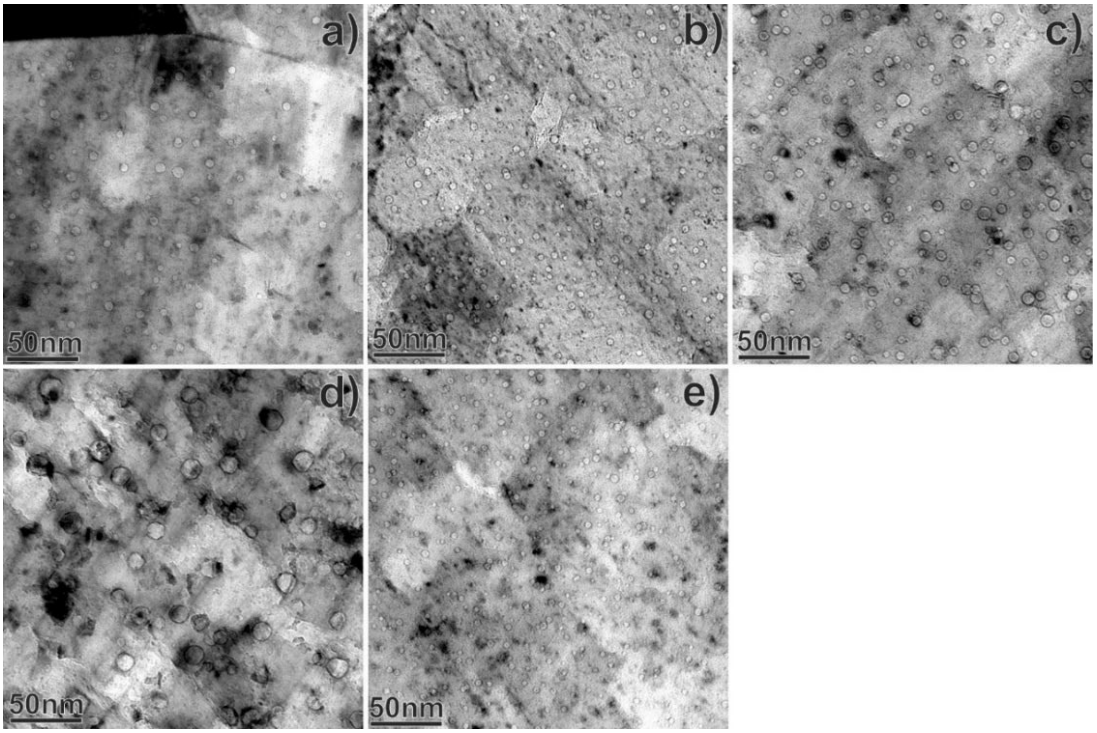


Figure 1: Bright-field TEM images showing voids in W irradiated at 600 °C (a), 900 °C (b), 1000 °C (c), 1100 °C (d) and 1200 °C (e).

The void size distributions are summarized in histograms shown in Figure 2. The histograms obtained for 600°C and 1200°C show nearly symmetric Gaussian shapes, while the distribution at 900°C and 1000°C shows an elongated left shoulder expressing the higher fraction of small voids. The voids formed at 1100°C show a clear bimodal size distribution with 2 maxima (Figure 1d). While the small void fraction has an average size of ~4 nm, the average size of the large void fraction is 13 nm (Figure 2d). The average void size was found to be in a narrow range between 4.5 nm and 7 nm for all irradiation temperatures, except the material irradiated at 1100 °C. The quantitative data on the voids obtained from these and similar TEM images are listed in Table 4 and their temperature dependence is plotted in Figure 13a.

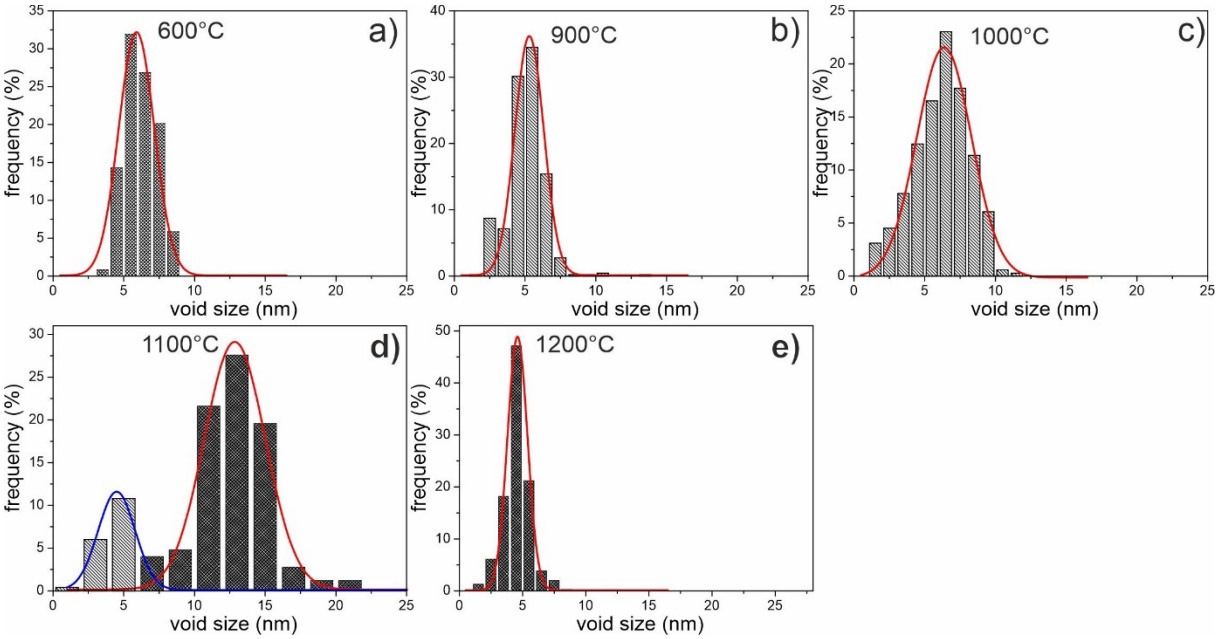


Figure 2: Size distribution histograms of the voids in W irradiated at various temperatures according to the TEM images shown in Figure 1.

## 3.2. Segregation of transmutation products

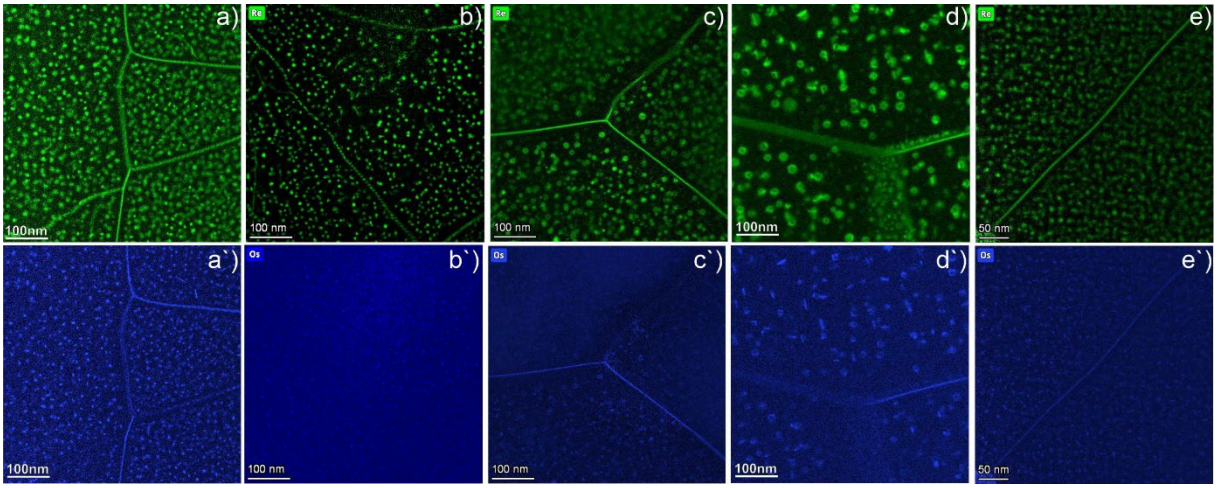


Figure 3: STEM-EDX spectrum images show the distribution of transmutation-induced Re (green) and Os (blue) inside W irradiated at 600 °C (a and a`), 900 °C (b and b`), 1000 °C (c and c`) 1100 °C (d and d`) and 1200 °C (e and e`).

Under the irradiation conditions in this study 2 % Re and 0.2 % Os were expected to be formed by transmutation. Their distribution was studied by STEM-EDX element mapping in the TEM, where the local presence of Re and Os was visualized by intensity variations of the different colors. Figure 3 demonstrates the distribution of Re (green) and Os (blue) in representative areas in the material irradiated at five temperatures. All maps were acquired at the same magnification. An exception are the maps of material irradiated at 1200 °C (e, e`), where the magnification was twice as high (see scale bars).

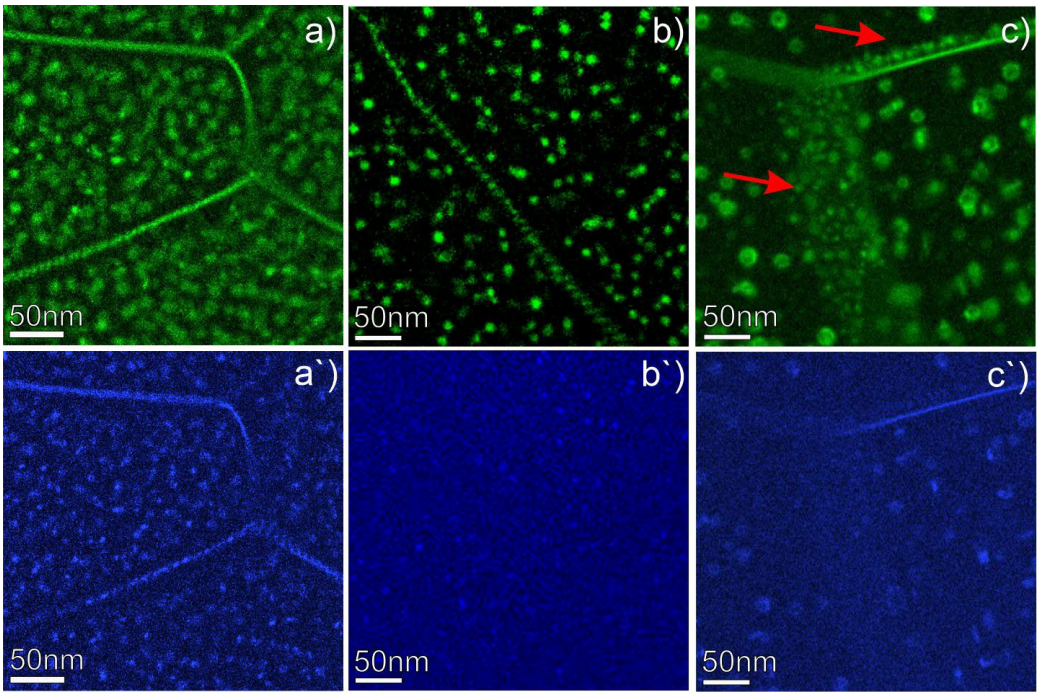


Figure 4: STEM-EDX spectrum images shows enlarged sections with grain boundaries from the maps of Figure 3. The distribution of transmutation induced Re (green) and Os (blue) inside W irradiated is shown for at 600 °C (a and a`), 900 °C (b and b`) and 1100 °C (c and c`) irradiation temperatures.

The elemental maps in Figure 3, 4 show the general distribution of transmutation elements on the large scale and are less useful for identifying concentration differences within individual clouds. The minor intensity variations are not well reproducible and identifiable in the color map. For this reason, we have used an intensity profile analysis across a typical void, precipitate and dislocation loop to show differences in Re and Os distribution in W irradiated at 600 °C (Figure 5). As mentioned above, these three defect types are typical nucleation sites in neutron irradiated W. The maps in Figure 5a-d demonstrate the distribution of W, Re, Os and combined Re/Os.

The elemental profile in Figure 5e shows that the Re intensity decreases slightly in the center, reflecting the position of the void. It should be noted that this intensity decrease can be seen on the voids of 5 nm and larger. For smaller voids, this effect is too weak to be imaged. Precipitates, on the contrary, show a higher local Re and Os concentration in the center (Figure 5e`). The Re and Os distribution around the dislocation loops can also be studied if the loops are larger than 15 nm and have an orientation in the image plane. The intensity profiles across the marked loop are plotted in Figure 5e``. It is notable that Re exhibits a uniform distribution in the area inside the loop, while Os tends to segregate at the dislocation line (Figure 5c,e``). Such clear results on dislocation loops are rare as the loops number density is significantly lower than other defects and they often overlap in TEM images with voids or precipitates.

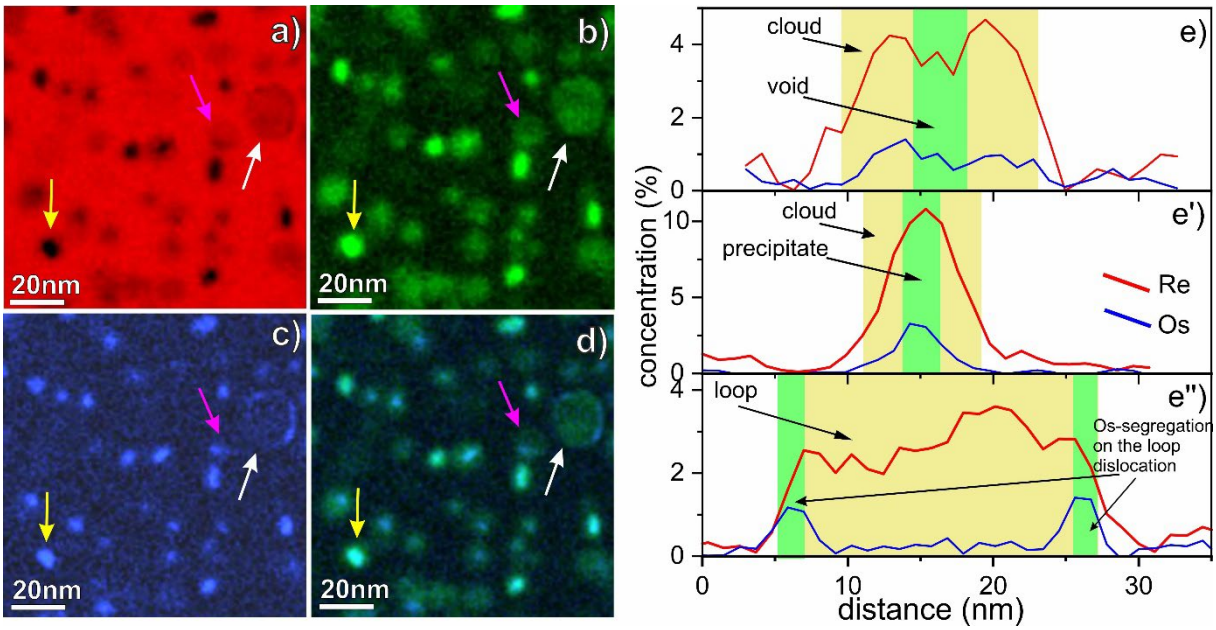


Figure 5: W, Re, Os and combined Re/Os elemental maps are shown in pars (a-d) for W irradiated at 600 °C. A void, a precipitate and a dislocation loop are marked in the maps with a magenta, yellow and white arrow, respectively. The corresponding Re and Os profiles intensity profile of these defect types are shown in parts (e-e``).

The precipitates are visible in HRTEM images, because their crystalline structure is different to that of W (see Table 2). Therefore, the microstructure of the precipitates (as recognizable in Figure 6a,b,c,d) were transformed by a Fast Fourier Transform (FFT) and shown separately in Figure 6a',b',c',d'.

The HRTEM image in Figure 6a illustrates a ~2 nm × 5 nm χ-$W(ReOs)_3$ precipitate with well-defined crystalline structure in the material irradiated at 600 °C. The χ-$W(ReOs)_3$ phase, which was clearly identified from the FFT images, is aligned with the $[111]_{\chi\text{-}W(ReOs)3}$ zone axis. The precipitate also has a well-defined orientation relationship with the W matrix, in particular $[110]_W \parallel [111]_{\chi\text{-}W(ReOs)3}$ zone-axes and $[00\bar{1}]_W \parallel [3\bar{3}0]_{\chi\text{-}W(ReOs)3}$ crystal directions are parallel to the image plane. Note that $d_{[011]W}$ and $d_{[330]\chi\text{-}W(ReOs)3}$ have the same spacing of 0.256 nm, so that the corresponding reflections overlap in the FFT image (Figure 6a').

The HRTEM image of a larger a ~3 nm × 11 nm precipitate from the same material is shown in Figure 6b. The FFT analysis proves that the structure of the precipitates has stacking faults in the direction $[1\bar{1}2]$ (Figure 6b`). This makes the clear identification of the crystalline phase impossible. It can be assumed that a defective χ-$W(ReOs)_3$ phase has formed here as well, since the reflections of the particle (blue rectangles in Figure 6b`) are very similar to the pattern shown in Figure 6a'. The presence of the stacking faults may be a result of the accommodation of the lattice strain misfit.

The ~4 nm thin and up to several tens of nanometers large precipitates, that are often located at voids, are formed in W irradiated at 1100 °C (Figure 6c). The corresponding FFT pattern obtained from the particle only is shown in Figure 6c`. The microstructure of the precipitate also exhibits typical stacking faults (as shown by the streaking in Figure 6b' and c'), but this

does not affect the identification of the correct reflection positions. The analysis shows that this particle consists of χ-$W(ReOs)_3$ phase and is oriented with the [113] zone axis.

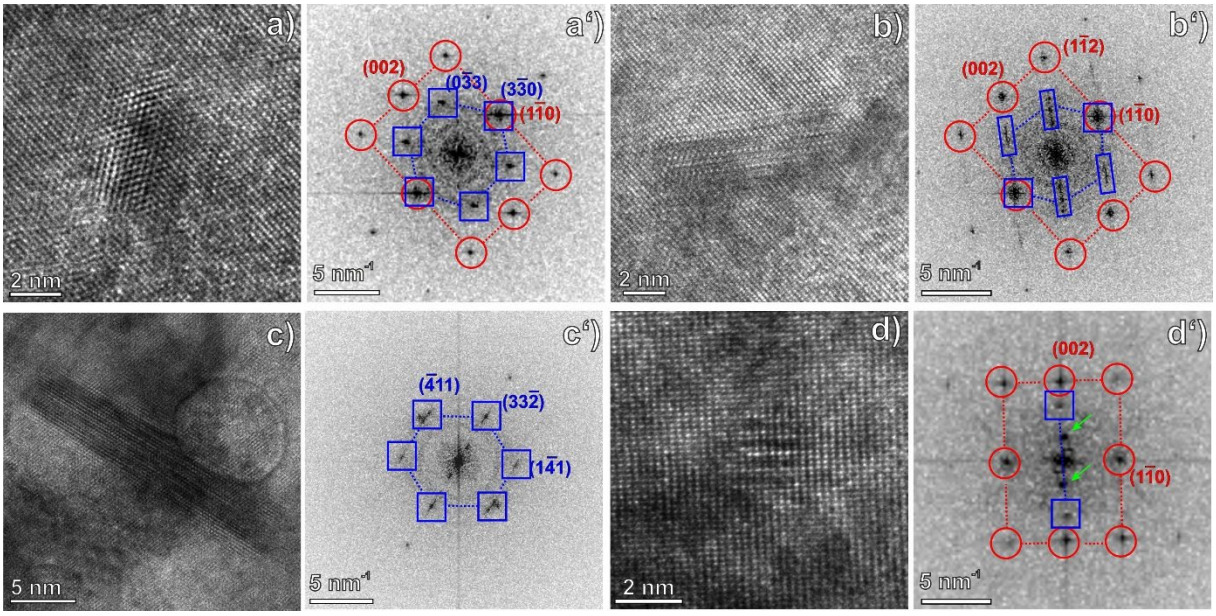


Figure 6: HRTEM images of nanoscale precipitates in W irradiated at 600 °C (a-b), 1100 °C (c) and 1200 °C (d). The corresponding Fast Fourier Transform (FFT) images are shown in parts (a'-d') accordingly. The diffraction spots of the W matrix are indicated by red circles, while the diffraction spots of the precipitations are marked by blue squares. The meaning of the green arrows in part 6d´is given in the text.

Nanometer sized precipitates were also found in the material irradiated at 1200 °C. The 2 nm large particle is imaged in the grain, aligned on the $[011]_W$ zone axis ( Figure 6d). The particle is only visible due to the translational Moiré fringes of ~0.5 nm periodicity, which results in spots that are marked by green arrows (Figure 6d`). This pattern originates from an interference of the W $[002]_W$ atomic planes ($d_{[200]} = 0.158$ nm) and an atomic plane from a precipitate having a periodicity of 0.24 nm (marked by blue squares in Figure 6d`). Reliable identification of the precipitation phase is not possible in this case since such atomic layers are present in both the σ- and χ-phase. Despite extensive efforts, we have not succeeded in finding a particle with two reflections that would allow unambiguous identification. It is also possible that particles with a size of a few lattice constants do not form a well-defined phase.

Measuring the concentration of elements in the clouds surrounding the voids or within precipitates is a difficult task because they are embedded in the W matrix. Nonetheless, the flash polishing procedure for surface cleaning allowed to separate the Re-Os-rich areas as replicas and, hence, enabled reliable analyses by TEM. This method makes use of differences in the chemical resistance of W-Re-Os precipitates and the surrounding pure W matrix against etching in NaOH solution. The etching rate for the "clouds" around the voids and precipitates is lower than for pure W, which in some cases results in the W matrix being completely removed while the Re-Os areas remain on a thin carbon film. The most successful preparation of this type was carried out on the sample irradiated at 1100 °C (Figure 7). Here, a BF-STEM image (part a) is shown with the corresponding W, Re and Os maps (b-d). The combined distribution of W and Re is shown in Figure 7e. The spatial distribution of Re and Os is very similar, the small differences in concentration in these elements are hardly distinguishable in the color

maps. Figure 7f shows W-, Re-, and Os-Lα EDX spectra with normalized intensity for pure tungsten (filled with red color and marked with a red arrow in (a)), clouds around voids (filled with blue color and marked with blue arrow in (a)) and precipitates (filled with green color and marked with green arrow in (a)). The overlapping spectra (in f)) illustrate differences in the composition of the precipitates and "clouds" with pure W.

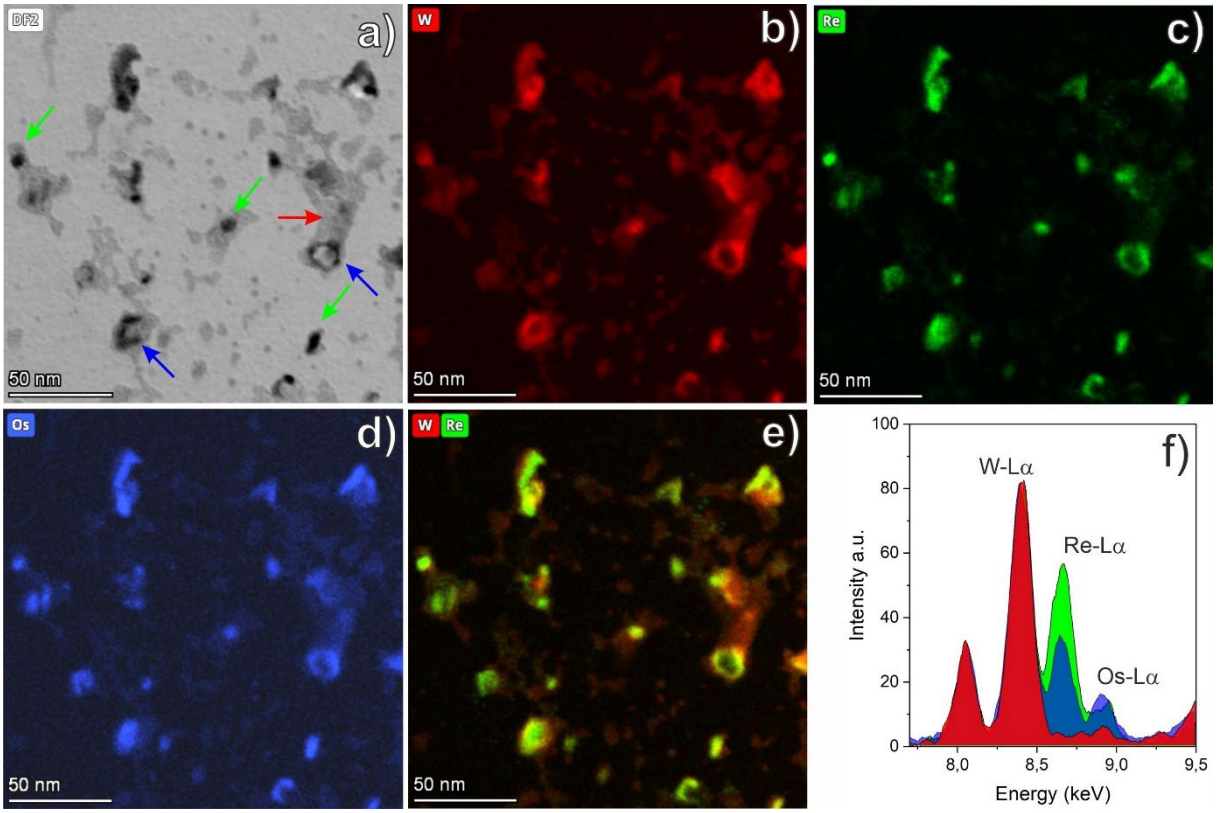


Figure 7: Analytical investigation of the Re/Os-rich clouds on the thin film. A STEM image (bright-field) of the investigated area is shown in part (a). Elemental maps of W (b), Re (c), Os (d) and combined W/Re map (e) illustrate the location of the elements. The EDX spectra with W-, Re-, Os-Lα lines obtained from the W matrix (red arrow in part (a)), particles (green arrows in part (a)) and “clouds” formed on voids (blue arrows in part (a)) are shown in part (f).

The compositions of the individual precipitates and "clouds" calculated based on the EDX spectra are listed in the Table 3. The values were determined as an average of about 10 measurements on different objects. The results show that the Re content in the precipitates is twice as high as in the clouds, while the Os content is approximately the same. The matrix contains nearly 100 at% W, the sub-percentage concentrations of Re and Os are within the error range.

Table 3: Quantification of extracted clouds and precipitates.

| Area | W (at%) | Re (at%) | Os (at%) |
|---|---|---|---|
| **W-matrix** | 99.4 | 0.2 | 0.4 |
| **clouds at the voids** | 67.0±3.0 | 21.6±1.5 | 11.4±1.0 |
| **precipitates** | 54.2±3.0 | 37.9±2.0 | 7.9±1.0 |

### 3.3. Dislocation loops

In addition to the voids and precipitates, dislocation loops are also generated in a considerable amount during neutron irradiation, which are visible mainly as small featureless black dots, as circular loops or as coffee-bean-like features. Figure 8 shows typical dislocation loops for samples irradiated at five different temperatures. The images were acquired in a g[110] two-beam condition. The nano-sized dislocation loops were found in all samples except for the one that was irradiated at 1100 °C (Figure 8d). This material also shows a different void and precipitate morphology, which is unique within all analyzed irradiation temperatures. For an irradiation temperature of 600 °C and 1200 °C, numerous black dots were observed in addition to the loops.

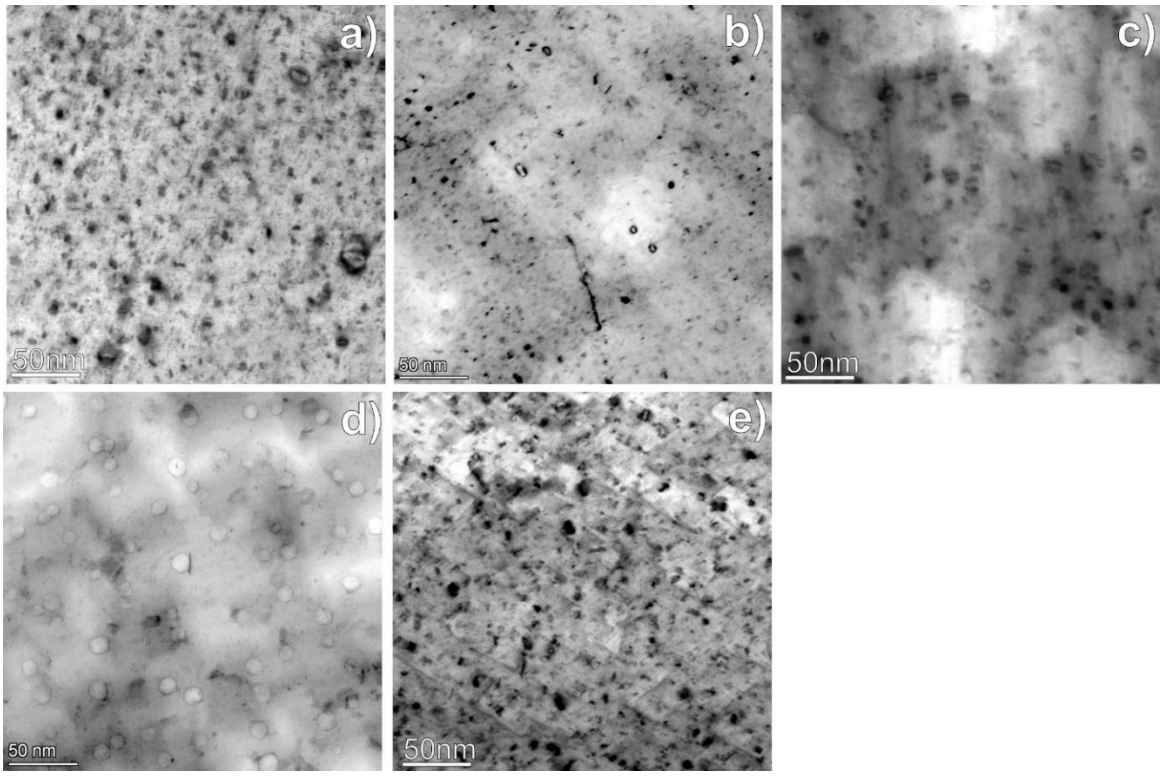


Figure 8: Visualization of dislocation loops and black dots using reverse contrast dark field (DF) imaging in W irradiated at 600 °C (part a), 900 °C (part b), 1000 °C (part c), 1100 °C (part d, showing only voids) and 1200 °C (part e). The DF images were obtained with g[110] g-vectors near the [110] or [100] zone-axes.

The identification and statistical evaluation of dislocation loops is very complicated and to some extent inaccurate, as they can be mistaken for the small precipitates that produce a similar contrast in the g-images (Figure 9). Figure 9a illustrates an area where several precipitates show the typical contrast with stacking faults. Such precipitates can be mistaken for dislocation loops in the overview images. Figure 9b,c, shows another region with dislocation loops imaged with the coffee bean contrast of 8-20 nm size (yellow arrows) and nanoscale precipitates (red arrows). These nanoscale precipitates could be interpreted as dislocation loops by mistake, as they have a loop-like shape. However, elemental mapping in Figure 9c shows that such “alleged loops” have an increased local Re concentration, which is comparable to the concentration measured for precipitates (Figure 7). The dislocation loops and voids, on the other hand, have

a much lower Re concentration around (Figure 5, Figure 9). For this reason, we only included loops that were clearly identified as loops, e.g., that had a coffee bean contrast, for the statistics. The results also confirm the Re-enrichment of the areas within the dislocation loops (yellow arrows).

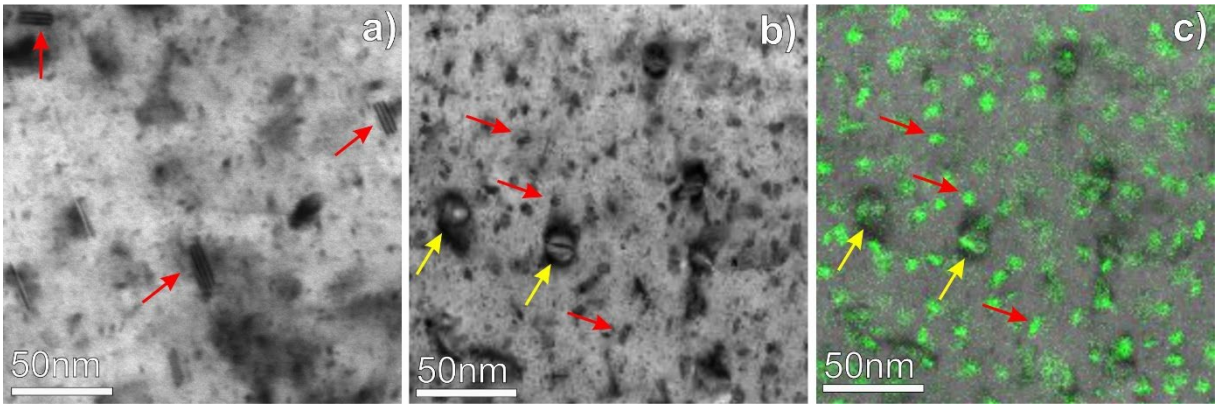


Figure 9: TEM images with precipitates (red arrows) (a), (b) and dislocation loops (yellow arrows) (b) in W irradiated at 600 °C. The image in part (c) is showing the same area as in (b) but with an overlapping Re map.

The determination of the Burgers vector of the dislocation loops was performed for samples irradiated at 600 °C (Figure 10), 900 °C (Figure 11) and at 1200 °C (Figure 12). The loop imaged in Figure 10a has either (100) or (010) habit plane and correspondingly $b\langle 100\rangle$ Burgers vector. The loop in the Fig. 11b has a (-111) habit plane and $b½\langle 111\rangle$ Burgers vector. Investigating more than 90 loops reveals that 85 % of them are of type $b½\langle 111\rangle$ and only 15% show a $b\langle 100\rangle$ Burgers vector. The application of the invisibility method to determine the Burgers vector proves not to be useful, as the loops could be mistaken for precipitates.

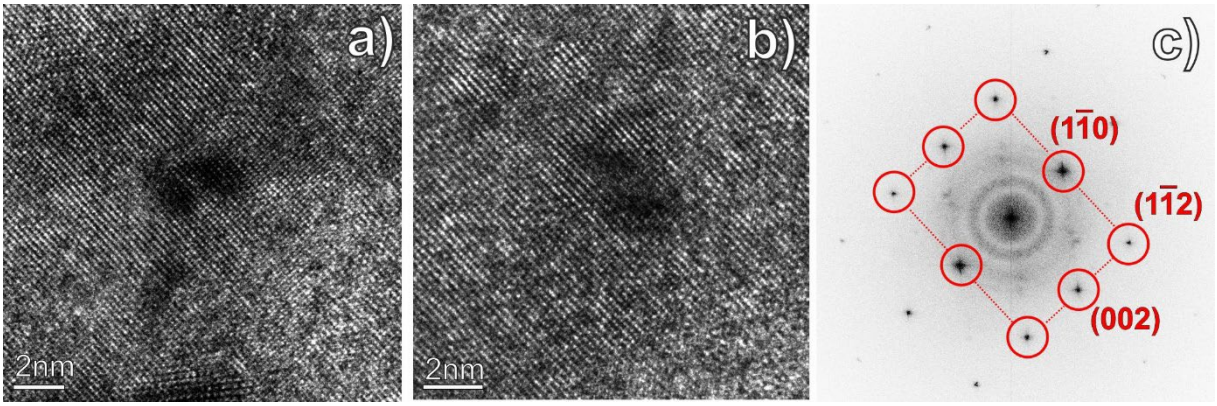


Figure 10: HRTEM imaging of dislocation loops in W irradiated at 600 °C (a,b). The corresponding FFT image, valid for both HRTEM images (a,b), is shown in part (c).

The application of the invisibility criterion was more successful for W irradiated at 900 °C (Figure 11). It could be demonstrated that the loops with both $b½\langle 111\rangle$ and $b\langle 100\rangle$ Burgers vectors are present in the material. As an example, the loop of $b½\langle 111\rangle$ type is marked with a

blue arrow and the loop of $b\langle 100\rangle$ type (red arrow), which is invisible in the g[-110] image (Figure 11b). The fraction of $b½\langle 111\rangle$ loops comprise about 75%.

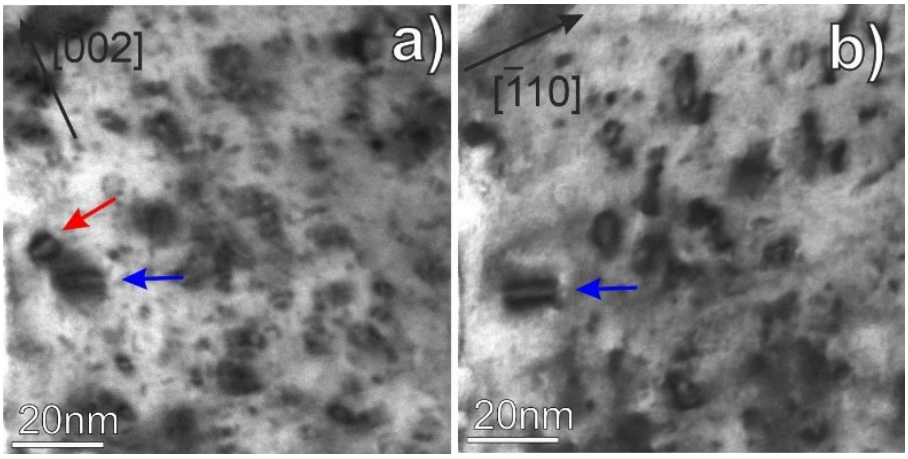


Figure 11: STEM images of the dislocation loops in W irradiated at 900 °C obtained with g[002] (a) and with g[-110] (b) near the [110] zone axis. The loop of $b½\langle 111\rangle$ type is marked by blue arrows, the loop of $b\langle 100\rangle$ type by a red one.

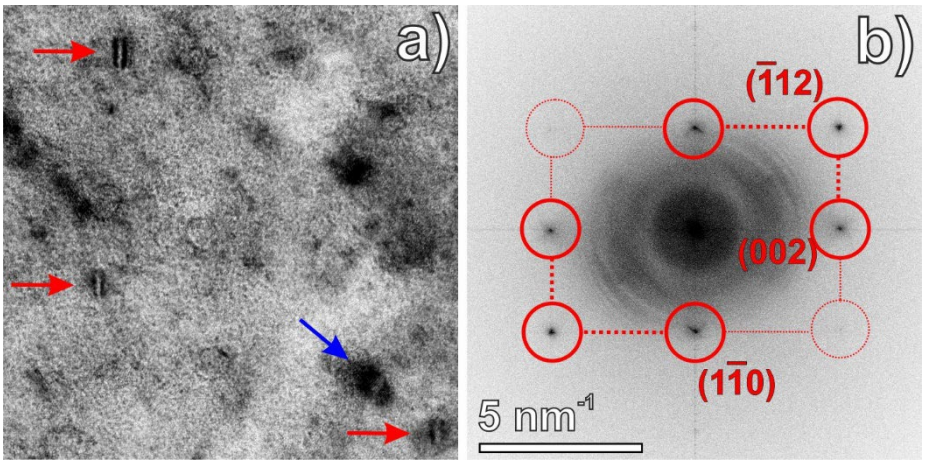


Figure 12: HRTEM imaging of dislocation loops in W irradiated at 1200 °C (a) and corresponding FFT image (b). The loop of $b½\langle 111\rangle$ type is marked by a blue arrow, the loops of $b\langle 100\rangle$ type by red ones (a).

Figure 12a displays dislocation loops in W irradiated at 1200 °C. Since the loops of $b\langle 100\rangle$ type show a projection into the image plane, which is typical for this zone axis, the orientation of the Burgers vector was determined by the use of HRTEM [22] rather than by STEM images. The fraction of loops with $b½\langle 111\rangle$ Burgers vector (blue arrow in Figure 12a) is only 25% at this irradiation temperature. This is significantly lower than for the lower irradiation temperatures. Quantitative data on the loops are presented in Table 4.

# 4. Discussion

The microstructural analysis shows the occurrence of voids, dislocation loops, and precipitates at all irradiation temperatures. The quantitative data on these defects, i.e., average size and number density, are listed in Table 4 and shown as graphs in Figure 13. The diagrams illustrate the temperature dependence of all relevant statistical parameters of radiation-induced defects in the range from 600 °C to 1200 °C. The average size, number density, and swelling were calculated for the void parameters. These parameters show similar values between 600 °C and 1000 °C and at the highest irradiation temperature of 1200 °C. It is noticeable that void size and number density show an inverse dependence to each other - the material with a larger void size has a lower number density (Figure 13a). In the sample irradiated at 1100 °C, voids show a significantly larger size, while the number density is 5 times lower than at the other temperatures. The void swelling shows a clear maximum with a value of ~1% at 1100 °C, while this value is 2-3 times lower at all other temperatures. This behavior is very similar to that reported by Matolich et al. [23], where the swelling maximum of 1.5% after 9.5 dpa was reported for irradiation temperatures between 800 °C to 900 °C. The void swelling of about 1% per dpa, obtained here at swelling peak temperature, surprisingly coincides with the swelling rate measured in steels and iron-based alloys also around the peak swelling temperature, as summarized by Garner et al [24].

Table 4: Quantitative and statistical data of voids and loops.

| | **voids** | | | **loops** | | | **precipitates** | |
|---|---|---|---|---|---|---|---|---|
| **$T_{irr}$** | average size (nm) | number density ($\times 10^{22}$ $m^{-3}$) | swelling (%) | average size (nm) | number density ($\times 10^{22}$ $m^{-3}$) | ½<111> loop fraction | average size (nm) | number density ($\times 10^{22}$ $m^{-3}$) |
| **600 °C** | 6.8 | 3.7 | 0.61 | 11.2 | 0.21 | 83% | 5 | 1.2 |
| **900 °C** | 5.0 | 6.7 | 0.44 | 5.4 | 2.5 | 75% | 2.5 | 0.6 |
| **1000 °C** | 6.2 | 6.2 | 0.77 | 6.5 | 3.7 | 80% | 3.7 | 0.62 |
| **1100 °C** | 11.3 | 1.2 | 0.91 | ------ | ------ | ------ | 12 | 1.3 |
| **1200 °C** | 4.5 | 8.5 | 0.32 | 4.7 | 0.75 | 25% | 2,3 | 0.53 |

Analytical investigations show that the voids are surrounded by 8-15 nm "clouds" at all temperatures, which have an enriched Os and Re content (Figure 3, Figure 4 and Figure 5). The "clouds" do not produce any diffraction contrast in TEM images and can only be visualized by analytical methods. Their study became possible only by the technical developments of the last decade, which have a significantly increased EDX sensitivity in TEM analysis [6]. In EDX spectra, the proportion of Re and Os in relation to W is typically near the sensitivity limit of the EDX method. In Figure 5, a cloud around a void is marked in corresponding elemental maps by magenta arrows. The Re and Os profiles across this void are plotted in Figure 5e. The Re-

profile shows a slight decrease in the center, reflecting the presence of a void in the center. A correlation between the size of the “clouds” and the irradiation temperature was not found.

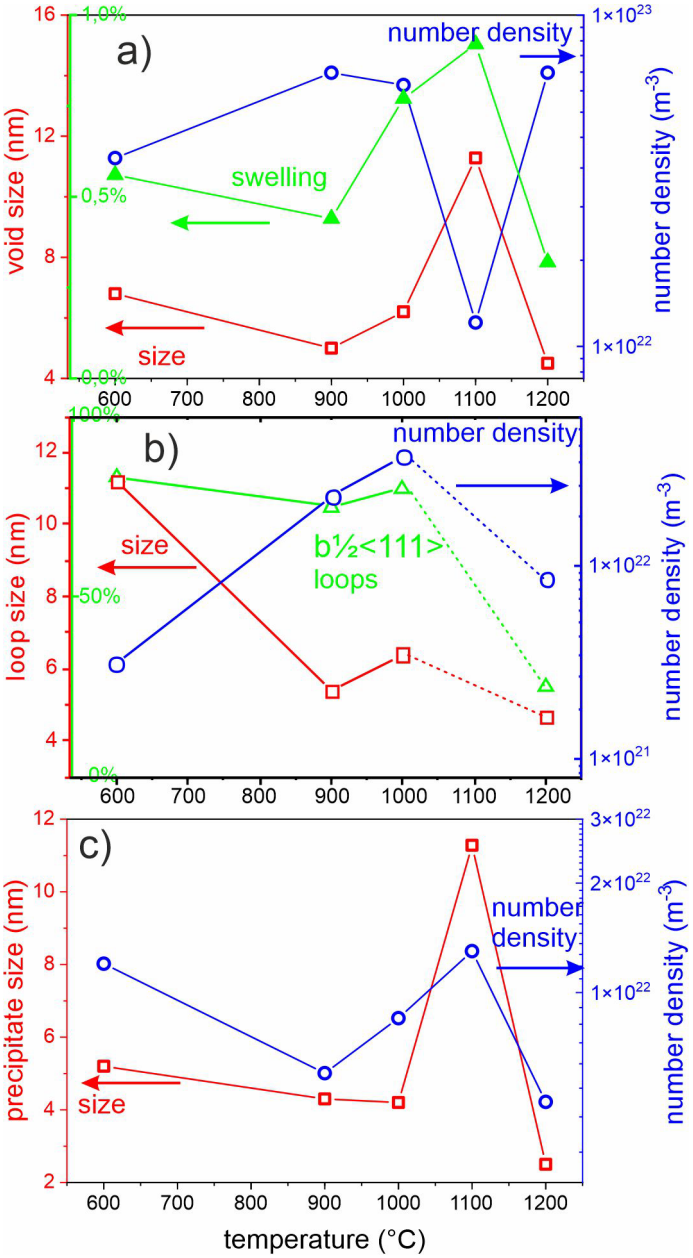


Figure 13: The diagrams show a temperature dependence of the void size (red color, left axis) and number density (blue color, right axis) (a). The green triangles indicate the temperature dependence of void swelling, where the y-axis ranges from 0 to 1% (Table 4). The temperature dependence of the site and number density of dislocation loops and precipitates are shown in parts (b) and (c), respectively.

The clouds are usually embedded in a W matrix, so that the actual local Re and Os contents are measured with a considerable error. The overlay effects from the matrix, which usually are present in the chemical analyses, could be avoided by the use of replicas from the clouds formed at 1000 °C. The values obtained from the analysis of the replica that is imaged in Figure 7 are compiled in Table 3. The measured Re and Os contents are higher than the values reported by

TEM analysis in Ref. [25] and by atomic probe tomography [3], where a Re concentration in the 8-10 at% range was reported. It can be assumed that the Re-Os content in the clouds depends to a large extent on the total Re-Os concentration in the sample and on the number density of the voids. The measurements on the replica can be compared with the APT analysis in terms of accuracy, since the objects are not embedded in the W-matrix. Lloyd et al. report that Os forms a core in the center of the clouds, at the interface between void and matrix, which might provide favorable conditions for a nucleus formation by precipitation [3]. The formation of an Os rich nucleus inside the cloud can be also derived from the Os intensity distribution across the void, which clearly shows a higher concentration at the void-matrix interface (Figure 5e).

In general, the Re and Os distribution and nucleation analyzed for all samples of W irradiated at different temperatures shows specific similarities and differences, which are summarized below and described and distinguished in more detail afterwards.

Similar features that are relevant for all irradiation temperatures:

- There are three segregation sites for Re and Os inside grains, which can be identified at all temperatures: (i) around voids and (ii) dislocation loops, and (iii) forming nano-sized precipitates with “clouds”.
- The segregation of Re and Os at grain boundaries and the formation of a 10-20 nm wide denuded zone on both sides of the grain boundary can be clearly seen.

Differences in the distributions for some temperatures:

- The precipitates form and grow independently of the voids (Figure 6a,b and c), with the exception of W irradiated at 1100 °C (Figure 6d), where elongated precipitates are associated with voids in most cases.
- At 1100 °C, it was found that in some cases Re does not form a continuous layer on the grain boundary, but rather closely located discrete spots of 5-10 nm size and of unknown nature (Figure 4c,c’ red arrows).
- At 600 °C and 900 °C it was observed that Re and Os segregate at grain boundary dislocations and not homogeneously distributed at the grain boundaries, as previously assumed [3,6]. This can be seen particularly well in Figure 4a,a’ and b,b’ in which an enlarged section with grain boundaries from the maps of Figure 3 is shown. Presumably, this effect is also present at higher temperatures, although it could not be clearly proven. For its visualization, the dislocations, which are often most visible in low angle grain boundaries, must be oriented perpendicular to the image plane. The fact that such a configuration is uncommon and not easily recognized in TEM images makes targeted studies more difficult.

The temperature dependence of important statistical data on dislocation loops is presented in Figure 13b. The size of the dislocation loops systematically decreases with the irradiation temperature, while their number density shows a maximum at 1000 °C. Dislocation loops were not detected at 1100 °C. Presumably, the larger voids and precipitates formed at 1100 °C have some influence on the loop formation.

The identification and statistical evaluation of dislocation loops involve considerable uncertainty because they can be mistaken for small precipitates that produce a similar contrast in the two-beam images. Figure 9a shows an area were several precipitates have a typical

contrast due to stacking faults. Such precipitates, especially with two lines, can be mistaken for dislocation loops in the overview images. In Figure 9b several dislocation loops of 8-20 nm in size are well visible due to the coffee-bean contrast. In HRTEM images, the precipitates show a defined crystalline structure and the loops a typical "coffee bean contrast" (Figure 10, Figure 12). However, HRTEM images can only be obtained from thin sample areas, and their analysis is complex. All the aforementioned factors affect the statistical data.

The Burgers vector analysis demonstrates that loops of both $b\langle 100\rangle$and $b\frac{1}{2}\langle 111\rangle$ types are present in W at all irradiation temperatures. The data showing the fraction of $b\frac{1}{2}\langle 111\rangle$-loops at different temperatures are listed in Table 4. At irradiation temperatures up to 1000 °C, 70-80% of the loops have a $b\frac{1}{2}\langle 111\rangle$Burgers vector. At 1200 °C the $b\langle 100\rangle$-loops became more dominant than $b\frac{1}{2}\langle 111\rangle$-loops, which fraction reduces to 25% Figure 13b.

So far, Burgers vector analysis of dislocation loops have been mainly reported for ion irradiated materials. In most of these cases the formation of $b\frac{1}{2}\langle 111\rangle$-loops was observed in W. However, the presence of a small amount (4% to 6%) of $b\langle 100\rangle$-loops was reported [26]. These results are consistent with our analysis, which shows that at lower irradiation temperatures 70%-80% of the loops have a $b\frac{1}{2}\langle 111\rangle$ Burgers vector and only a small fraction has a $b\langle 100\rangle$ Burgers vector. In the present work, we show that mainly $b\langle 100\rangle$-loops form at 1200 °C. This result suggests a similarity in the dislocation loop formation between Fe-Cr alloys and W (both materials have a bcc lattice structure). Post irradiation examination of EUROFER97 (9Cr-1W-VTa steel) reveals that $b\langle 100\rangle$ loops form preferentially above 350 °C, while $b\frac{1}{2}\langle 111\rangle$ loops dominate at lower irradiation temperatures [27]. In W, however, this effect is attributed to a higher irradiation temperature and $b\langle 100\rangle$ loops become dominant somewhere between 1000 °C and 1200 °C. Strikingly, when normalized to the melting temperature $T_m$ (i.e., by applying homologous temperatures), this transition of dominant loops is very similar for Fe-9Cr-1W-VTa at 0.36 $T_m$ and for W between 0.35 $T_m$ and 0.40 $T_m$. In the few publications where the nature of dislocation loops has been investigated experimentally, it has been shown that the loops in W have mostly interstitial nature [28,29]. The observed formation of vacancy loops of $b\langle 100\rangle$-type was reported only in one case [29].

In general, it is well known that ½<111> loops are highly mobile in BCC metals, as for instance was experimentally evidence by Arakawa et al. [30]. Hence, the observation of the loops after the irradiation at high temperature must be related to the immobilization caused by the presence of carbon and segregation of Re and Os [31,32]. The latter effect may play a major role as the results presented here clearly indicate the strong segregation of Re and Os at loops. Given that at 1100 C irradiation, the microstructure is dominated by voids which also getter Re and Os atoms, the confinement of the loops might not be sufficient to avoid loop diffusion and sinking at natural defects such as dislocations and grain boundaries. At 1200 C, the thermal stability of voids is reduced, their density is becoming lower and correspondingly more Re/Os becomes available to confine the loops. This interplay may explain why the loops were not observed at 1100 C.

Another important remark is to be made about the mechanisms of the loop formation and growth. The dominant formation of <100> loops in the most studied BCC metal iron has been noted at higher temperatures (above 0.35 $T_m$, as noted above), while at lower irradiation temperatures the formation of ½<111> loops prevailed. In the case of Fe, Dudarev has proposed

an explanation based on the magnetic nature of the iron and interplay of the free formation energy [33]. However, such explanation did not justify the observation of the <100> loops in Fe-Cr alloys and ferritic steels. Alternative explanation was based on the formation of the <100> loops as a result of the direct reaction between two ½<111> loops [34]. The latter mechanism implies that the loop-loop interaction leads to the formation of <100> loops but with a certain energy barrier, which is why these defects are observed only above specific temperature, and which is also why ½<111> loops are scarce at high irradiation temperature unless certain immobilization mechanisms is present. Given that tungsten is paramagnetic material up to the melting point, the results of this work can be interpreted in support of the loop-loop interaction mechanism as we clearly see the strong reduction of the fraction of ½<111> loops as irradiation temperature start to exceed 0.3 $T_m$.

Figure 5c shows the enrichment of Re and Os on both voids and dislocation loops forming often small areas with higher Os concentration. This implies that loops might serve as nucleation sites for precipitates in addition to voids. While the voids on the precipitates are usually well visible [25], the loops next to the grown precipitates are hardly detectable or simply disappear if the precipitate size increases. In addition, precipitates in W irradiated at 1100°C have a significantly larger size and higher number density than at other irradiation temperatures (Figure 13), so there are more sites for recombination of interstitial defects which high concentration is necessary for loop formation. Given that the atomic density of the σ-$WOs_2$ and χ–$WRe_3$ precipitates is higher than the atomic density of bcc W by 2.7% and 4.1%, respectively, the formation of precipitates comes in volumetric balance with the formation voids i.e. atoms left their sites to create voids contribute to the growth of the precipitates. In this situation, the freshly in-cascade created dislocation loops and self-interstitial clusters would contribute to the further growth of the precipitates. Together, these two effects could explain the absence of dislocation loops in the sample with the largest void fraction.

EDX elemental maps show that Re and Os segregation takes place inside single dislocation loops (Figure 5, Figure 9). However, the loops are two-dimensional objects and consequently the Re and Os distribution is also two-dimensional. In Figure 5a, a dislocation loop with a diameter of 20 nm, which projects a circular area onto the image plane, is marked by a white arrow in the elemental maps. The line scan across a loop is shown in Figure 5e''. It is evident that Re is uniformly distributed inside the loops, while Os tends to segregate along the dislocation line. Such a Re segregation was also detected on dislocation loops, which are inclined to the image plane (Figure 8). These measurements were performed near the detection limit of EDX spectroscopy and are infrequent in such clarity due to two reasons: (i) it is rare that loops can be imaged with a circular projection without overlapping with voids or precipitates, and (ii) the loops should be located within a thin sample region for an optimal signal-to-noise ratio (SNR). In addition to a poor SNR, in thicker TEM foils the probability for loops overlapping with other sample features is increased. This hampers the detection of the above-mentioned effects. Similar re- and Os-segregation on dislocation loops was described by M.J. Lloyd et al [35], with ATP measurements underpinned by corresponding FISPACT-II simulations.

Dislocation loops in W were already observed after a neutron irradiation dose of only 0.03 dpa at an irradiation temperature of 90 °C [8]. As reported in previous studies [29,36–38], they

appear up to 900 °C irradiation temperature. The recently published temperature-damage diagrams cover the irradiation temperature range from 100 °C to 900 °C and for damage doses of up to 2 dpa [39]. Our results show the presence of dislocation loops at 1200 °C, which is also consistent with results published by other groups [40].

The third type of radiation-induced defects are the W-Re-Os precipitates, which were found to form at all considered irradiation temperatures. The derived statistical data on precipitates are presented in Figure 13c. The average size is usually smaller than 5 nm, except for W irradiated at 1100 °C, where the size of the precipitates is larger than 10 nm (Figure 6). The location of the precipitates was found to be mainly independent on the voids, with the exception of W irradiated at 1100 °C. It can be assumed that the concentration of transmutation products (Re and Os) does not reach the level at which precipitates are formed in clouds around the voids. The number density of precipitates reaches a maximum at 1100 °C (Figure 13c).

An example of a precipitate is marked with a yellow arrow in Figure 5. In the elemental maps, the precipitate shows a clear Re and Os intensity maximum in the center, which is surrounded by a cloud with lower Re and Os concentrations (Figure 5e'). The Re and Os distributions show a clear difference to the distributions around voids, which are visible as diffuse clouds with a slight reduction of intensity at their center (Figure 5e).

HRTEM analysis shows that the precipitates have a crystalline structure even at a size of about 2 nm (Figure 6d,d'). Figure 6a,a' presents HRTEM analysis of a 4 nm precipitate in W irradiated at 600 °C. The hexagonal FFT pattern with an atomic spacing of 0.226 nm corresponds very well to the cubic $\chi$-$WRe_3$ phase. It should be emphasized that the dimension of such precipitates measures only 3-5 lattice constants and, therefore, they probably have a distorted structure depending on the lattice misfit with the surrounding W matrix. An increase of the precipitates to 10 nm is accompanied by the formation of stacking faults (Figure 5b, b'). The structure of such particles cannot be clearly identified using HRTEM, because the position of the diffraction points cannot be precisely determined due to spot streaking. In the given example, it can be suggested that the spots have the same position as in Figure 5a,a' and, hence, the particle would also represent $\chi$-$W(ReOs)_3$ phase. In W irradiated at 1100 °C, the particle size increased to 30 nm (Figure 5c,c'). Despite the accompanied stacking faults, here the position of the diffraction spots can be determined with an acceptable error. Thus, it can be suggested that the structure corresponds to the $\chi$-$W(ReOs)_3$ phase as well.

The precipitates that form at 1200 °C typically have a size of just 1-2 nm. Such small particles are visible only on the basis of their crystal structure, which is different from that of the bulk W. In HRTEM images, such particles are imaged by one atomic line only, making phase identification even more problematic. However, it was possible to resolve the structure of a 4 nm large particle that nearly corresponds to the $\chi$-$W(ReOs)_3$ phase. The main problem here is the embedding of the particles in the W matrix and the resulting double diffraction spots that could be mistaken for real structures.

In tungsten, radiation induced migration of Re and Os atoms obviously leads to the formation of precipitates. Thus, the mobility and the binding mechanism of solute atoms to defects are considered the most appropriate explanation for radiation-induced precipitation [41–43]. Both vacancies and self-interstitial atoms (SIA) are able to drag solute atoms, while the contribution of the SIAs to the aggregation of the solute atoms is much greater than the vacancies [43]. It

was shown that solutes such as Re or Os are much more strongly bound to interstitial sites than to voids. Interstitial solute complexes were found to be very effective in enriching solutes at sinks, such as voids or already formed precipitates. The enrichment of Re and Os around voids and the formation of precipitates is experimentally validated in the present work.

Grain boundaries play an important role in the formation and coarsening of radiation-induced defects (Figure 3, Figure 4). They act as sinks for all kinds of point defects, i.e., for vacancies and interstitials as well as, in our case, for Re and Os atoms, resulting in the formation of a 10-20 nm wide zone, adjacent to the grain boundaries, which is free of voids and precipitates (the so-called denuded zone). In addition, we found that Re and Os are often inhomogeneously distributed along grain boundaries which is due to segregation at boundary dislocations (Figure 4). This is also consistent with our recent results, where Os segregation at the dislocation loops was demonstrated.

In general, experimental data collected in recent years shows that the microstructure of neutron-irradiated W depends on the temperature and the damage dose, as well as on the concentration of transmutation products. For the latter one, the applied neutron spectrum is of great importance, which itself is different for each reactor type and which depends on the shielding factor, the position of the sample in the irradiation rig, and the rig design. Our analyses form the basis for a more in-depth understanding of the microstructural development of W under neutron irradiation. However, considerably more research is required to uncover all possible structural effects that might occur in a nuclear fusion reactor.

When analyzing the results of W irradiation in different reactors, significant differences in the size and distribution of the voids can be found. For example, in pure W with a grain size of 13.5µm, after irradiation in the JOYO fast reactor to the doses higher than 1.5 dpa, voids were formed by a number density in the $10^{23}$ $m^{-3}$ range. Fukuda et al. [44] shows, for example, that the number density in pure W irradiated at 537 °C is $1.9\times10^{23}$ $m^{-3}$. A similar values of $1.2\times10^{23}$ $m^{-3}$ (750 °C, 1.54 dpa) and $5\times10^{23}$ $m^{-3}$ (538 °C, 0.9 dpa) was reported by Tanno et al. [38,45]. The formation of void lattices with 20 nm spacing in the damage dose from 0.40 to 1.54 dpa at 538 °C and 750 °C in pure W was reported in references [46,47]. In contrast to these examinations, the formation of void lattice was not observed in the present study. However, as has been recently studied by means of the computational modelling, the formation of the void lattice is sensitive to a number of factors such as initial microstructure, sink strength and trapping of loops [48]. The fast neutron spectrum in the JOYO reactor has a low cross-section for the transmutation of W into Re and Os, and, thus, the changes of the chemical composition during irradiation are negligible, at least for such low doses as considered here.

Precipitates containing Re and Os are also formed in pure W irradiated in the HFIR. Due to the high flux of thermal neutrons, the nuclear transmutation rate in HFIR is much higher than in JOYO. The material analyzed in our work (irradiated in the BR-2 reactor) shows the presence of ~2 at% Re and ~0.2 at% Os after irradiation to 0.8 dpa. Therefore, the transmutation rate of ~1.6 at% Re/dpa is similar to that calculated for HFIR reactors by Greenwood and Garner [49]. The formation of precipitates with defined stoichiometric composition and crystalline structure starts when the irradiation temperatures exceed 500 °C and leads to the formation of σ-$WRe_2$ and χ-$WRe_3$ phases [7,45]. In particular, it was reported that the χ-phase has a needle-like shape

and the σ-phase has a spherical shape [36,38]. This was also confirmed in the present work where only formation of χ-$WRe_3$ precipitates was observed.

## Conclusions

This study presents the results of extensive microstructural analyses of W samples, which were neutron irradiated at temperatures between 600 °C and 1200 °C, up to a damage dose of ~0.8 dpa. The formation of dislocation loops, voids, and precipitates consisting of Re-Os χ-phases was observed and characterized in detail. The results of the study can be summarized as follows:

- Voids were detected at all irradiation temperatures. The void swelling, measured for low and high irradiation temperatures, amounts to about 0.3-0.4% and shows a maximum of about 0.8-1.0% at 1000 °C-1100 °C.
- The microstructure of W irradiated at 1100 °C differs significantly from that of the other irradiation temperatures. The differences include noticeably larger voids and precipitates and thus strong void swelling, as well as the absence of dislocation loops.
- Dislocation loops with small sizes were detected at all temperatures, except for 1100 °C. It was found that loops with a Burgers vector of type $b½\langle 111\rangle$ dominate at temperatures below 1100 °C, while at 1200 °C the majority of loops have $b\langle 100\rangle$ Burgers vector.
- The nanoscale precipitates of χ-phases were detected at all irradiation temperatures. A considerable fraction of the precipitates grows with stacking faults, so that their phase cannot be unambiguously identified.
- Voids, dislocation loops, and precipitates serve as sinks for point defects which transfer transmutation induced Re and Os. Their enrichment at dislocation loops was detected for the first time.

## Acknowledgements

This work has been carried out within the framework of the EUROfusion Consortium and has received funding from the Euratom research and training programme 2014-2018 and 2019-2020 under grant agreement No 633053. The views and opinions expressed herein do not necessarily reflect those of the European Commission.

## References

**References**

[1] H. Bolt, V. Barabash, W. Krauss, J. Linke, R. Neu, S. Suzuki, N. Yoshida, A.U. Team, Materials for the plasma-facing components of fusion reactors, Journal of Nuclear Materials 329-333 (2004) 66–73. https://doi.org/10.1016/j.jnucmat.2004.04.005.

[2] M. Rieth, R. Doerner, A. Hasegawa, Y. Ueda, M. Wirtz, Behavior of tungsten under irradiation and plasma interaction, Journal of Nuclear Materials 519 (2019) 334–368. https://doi.org/10.1016/j.jnucmat.2019.03.035.

[3] M.J. Lloyd, R.G. Abernethy, M.R. Gilbert, I. Griffiths, P.A. Bagot, D. Nguyen-Manh, M.P. Moody, D.E. Armstrong, Decoration of voids with rhenium and osmium transmutation products in neutron irradiated single crystal tungsten, Scripta Materialia 173 (2019) 96–100. https://doi.org/10.1016/j.scriptamat.2019.07.036.
[4] A. Hasegawa, M. Fukuda, K. Yabuuchi, S. Nogami, Neutron irradiation effects on the microstructural development of tungsten and tungsten alloys, Journal of Nuclear Materials 471 (2016) 175–183. https://doi.org/10.1016/j.jnucmat.2015.10.047.
[5] T. Hwang, A. Hasegawa, K. Tomura, N. Ebisawa, T. Toyama, Y. Nagai, M. Fukuda, T. Miyazawa, T. Tanaka, S. Nogami, Effect of neutron irradiation on rhenium cluster formation in tungsten and tungsten-rhenium alloys, Journal of Nuclear Materials 507 (2018) 78–86. https://doi.org/10.1016/j.jnucmat.2018.04.031.
[6] M. Klimenkov, U. Jäntsch, M. Rieth, H.C. Schneider, D. Armstrong, J. Gibson, S.G. Roberts, Effect of neutron irradiation on the microstructure of tungsten, Nuclear Materials and Energy 9 (2016) 480–483. https://doi.org/10.1016/j.nme.2016.09.010.
[7] A. Hasegawa, M. Fukuda, S. Nogami, K. Yabuuchi, Neutron irradiation effects on tungsten materials, Fusion Engineering and Design 89 (2014) 1568–1572. https://doi.org/10.1016/j.fusengdes.2014.04.035.
[8] T. Koyanagi, N.K. Kumar, T. Hwang, L.M. Garrison, X. Hu, L.L. Snead, Y. Katoh, Microstructural evolution of pure tungsten neutron irradiated with a mixed energy spectrum, Journal of Nuclear Materials 490 (2017) 66–74. https://doi.org/10.1016/j.jnucmat.2017.04.010.
[9] J.-H. You, A review on two previous divertor target concepts for DEMO: mutual impact between structural design requirements and materials performance, Nucl. Fusion 55 (2015) 113026. https://doi.org/10.1088/0029-5515/55/11/113026.
[10] T. Loewenhoff, A. Bürger, J. Linke, G. Pintsuk, A. Schmidt, L. Singheiser, C. Thomser, Evolution of tungsten degradation under combined high cycle edge-localized mode and steady-state heat loads, Phys. Scr. T145 (2011) 14057. https://doi.org/10.1088/0031-8949/2011/T145/014057.
[11] A. Dubinko, D. Terentyev, A. Bakaeva, K. Verbeken, M. Wirtz, M. Hernández-Mayoral, Evolution of plastic deformation in heavily deformed and recrystallized tungsten of ITER specification studied by TEM, International Journal of Refractory Metals and Hard Materials 66 (2017) 105–115. https://doi.org/10.1016/j.ijrmhm.2017.03.004.
[12] M. Zibrov, M. Balden, M. Dickmann, A. Dubinko, W. Egger, M. Mayer, D. Terentyev, M. Wirtz, Erratum: Deuterium trapping by deformation-induced defects in tungsten (2019 Nucl. Fusion59 106056), Nucl. Fusion 59 (2019) 129601. https://doi.org/10.1088/1741-4326/ab472b.
[13] D.B. Pelowitz, J.W. Durkee, J.S. Elson, M.L. Fensin, J.S. Hendricks, M.R. James, R.C. Johns, G.W. Mc Kinney, S.G. Mashnik, L.S. Waters, T.A. Wilcox, J.M. Verbeke, MCNPX 2.7.0 extensions, 2011.
[14] A. Konobeyev, U. Fischer, Y. Korovin, S.P. Simakov, Evaluation of effective threshold displacement energies and other data required for the calculation of advanced atomic displacement cross-sections, Nuclear Energy and Technology 3 (2017) 169–175. https://doi.org/10.1016/j.nucet.2017.08.007.
[15] A.J.M. Plompen, O. Cabellos, C. de Saint Jean, M. Fleming, A. Algora, M. Angelone, P. Archier, E. Bauge, O. Bersillon, A. Blokhin, F. Cantargi, A. Chebboubi, C. Diez, H. Duarte, E. Dupont, J. Dyrda, B. Erasmus, L. Fiorito, U. Fischer, D. Flammini, D. Foligno, M.R. Gilbert, J.R. Granada, W. Haeck, F.-J. Hambsch, P. Helgesson, S. Hilaire, I. Hill, M. Hursin, R. Ichou, R. Jacqmin, B. Jansky, C. Jouanne, M.A. Kellett, D.H. Kim, H.I. Kim, I. Kodeli, A.J. Koning, A.Y. Konobeyev, S. Kopecky, B. Kos, A. Krása, L.C. Leal, N. Leclaire, P. Leconte, Y.O. Lee, H. Leeb, O. Litaize, M. Majerle,

J.I. Márquez Damián, F. Michel-Sendis, R.W. Mills, B. Morillon, G. Noguère, M. Pecchia, S. Pelloni, P. Pereslavtsev, R.J. Perry, D. Rochman, A. Röhrmoser, P. Romain, P. Romojaro, D. Roubtsov, P. Sauvan, P. Schillebeeckx, K.H. Schmidt, O. Serot, S. Simakov, I. Sirakov, H. Sjöstrand, A. Stankovskiy, J.C. Sublet, P. Tamagno, A. Trkov, S. van der Marck, F. Álvarez-Velarde, R. Villari, T.C. Ware, K. Yokoyama, G. Žerovnik, The joint evaluated fission and fusion nuclear data library, JEFF-3.3, Eur. Phys. J. A 56 (2020). https://doi.org/10.1140/epja/s10050-020-00141-9.

[16] C. Yin, D. Terentyev, T. Zhang, R.H. Petrov, T. Pardoen, Impact of neutron irradiation on the strength and ductility of pure and ZrC reinforced tungsten grades, Journal of Nuclear Materials 537 (2020) 152226. https://doi.org/10.1016/j.jnucmat.2020.152226.

[17] E. Gaganidze, A. Chauhan, H.-C. Schneider, D. Terentyev, G. Borghmans, J. Aktaa, Fracture-mechanical properties of neutron irradiated ITER specification tungsten, Journal of Nuclear Materials 547 (2021) 152761. https://doi.org/10.1016/j.jnucmat.2020.152761.

[18] S. Hasanzadeh, R. Schäublin, B. Décamps, V. Rousson, E. Autissier, M.F. Barthe, C. Hébert, Three-dimensional scanning transmission electron microscopy of dislocation loops in tungsten, Micron (Oxford, England 1993) 113 (2018) 24–33. https://doi.org/10.1016/j.micron.2018.05.010.

[19] C.T. Rueden, J. Schindelin, M.C. Hiner, B.E. DeZonia, A.E. Walter, E.T. Arena, K.W. Eliceiri, ImageJ2: ImageJ for the next generation of scientific image data, BMC bioinformatics 18 (2017) 529. https://doi.org/10.1186/s12859-017-1934-z.

[20] P.A. Stadelmann, EMS - a software package for electron diffraction analysis and HREM image simulation in materials science, Ultramicroscopy 21 (1987) 131–145. https://doi.org/10.1016/0304-3991(87)90080-5.

[21] M. Klimenkov, P. Vladimirov, U. Jäntsch, V. Kuksenko, R. Rolli, A. Möslang, N. Zimber, New insights into microstructure of irradiated beryllium based on experiments and computer simulations, Sci Rep 10 (2020). https://doi.org/10.1038/s41598-020-64654-5.

[22] B. Yao, D.J. Edwards, R.J. Kurtz, TEM characterization of dislocation loops in irradiated bcc Fe-based steels, Journal of Nuclear Materials 434 (2013) 402–410. https://doi.org/10.1016/j.jnucmat.2012.12.002.

[23] J. Matolich, H. Nahm, J. Moteff, Swelling in neutron irradiated tungsten and tungsten-25 percent rhenium, Scripta Metallurgica 8 (1974) 837–841. https://doi.org/10.1016/0036-9748(74)90304-4.

[24] F. Garner, M. Toloczko, B. Sencer, Comparison of swelling and irradiation creep behavior of fcc-austenitic and bcc-ferritic/martensitic alloys at high neutron exposure, Journal of Nuclear Materials 276 (2000) 123–142. https://doi.org/10.1016/S0022-3115(99)00225-1.

[25] M. Dürrschnabel, M. Klimenkov, U. Jäntsch, M. Rieth, H.C. Schneider, D. Terentyev, New insights into microstructure of neutron-irradiated tungsten, Sci Rep 11 (2021) 7572. https://doi.org/10.1038/s41598-021-86746-6.

[26] R.W. Harrison, J.A. Hinks, S.E. Donnelly, Influence of pre-implanted helium on dislocation loop type in tungsten under self-ion irradiation, Scripta Materialia 150 (2018) 61–65. https://doi.org/10.1016/j.scriptamat.2018.02.040.

[27] M. Klimenkov, U. Jäntsch, M. Rieth, A. Möslang, Correlation of microstructural and mechanical properties of neutron irradiated EUROFER97 steel, Journal of Nuclear Materials 538 (2020) 152231. https://doi.org/10.1016/j.jnucmat.2020.152231.

[28] F. Ferroni, X. Yi, K. Arakawa, S.P. Fitzgerald, P.D. Edmondson, S.G. Roberts, High temperature annealing of ion irradiated tungsten, Acta Materialia 90 (2015) 380–393. https://doi.org/10.1016/j.actamat.2015.01.067.

[29] X. Hu, T. Koyanagi, M. Fukuda, N.K. Kumar, L.L. Snead, B.D. Wirth, Y. Katoh, Irradiation hardening of pure tungsten exposed to neutron irradiation, Journal of Nuclear Materials 480 (2016) 235–243. https://doi.org/10.1016/j.jnucmat.2016.08.024.
[30] K. Arakawa, T. Amino, H. Mori, Direct observation of the coalescence process between nanoscale dislocation loops with different Burgers vectors, Acta Materialia 59 (2011) 141–145. https://doi.org/10.1016/j.actamat.2010.09.018.
[31] N. Castin, A. Bakaev, D. Terentyev, M.I. Pascuet, G. Bonny, Understanding why dislocation loops are visible in transmission electron microscopy: The tungsten case, Journal of Nuclear Materials 555 (2021) 153122. https://doi.org/10.1016/j.jnucmat.2021.153122.
[32] N. Castin, P. Dwivedi, L. Messina, A. Bakaev, D. Terentyev, G. Bonny, The effect of rhenium on the diffusion of small interstitial clusters in tungsten, Computational Materials Science 177 (2020) 109580. https://doi.org/10.1016/j.commatsci.2020.109580.
[33] S.L. Dudarev, R. Bullough, P.M. Derlet, Effect of the alpha-gamma phase transition on the stability of dislocation loops in bcc iron, Physical review letters 100 (2008) 135503. https://doi.org/10.1103/PhysRevLett.100.135503.
[34] H. Xu, R.E. Stoller, Y.N. Osetsky, D. Terentyev, Solving the puzzle of <100 interstitial loop formation in bcc Iron, Physical review letters 110 (2013) 265503. https://doi.org/10.1103/PhysRevLett.110.265503.
[35] M.J. Lloyd, A.J. London, J.C. Haley, M.R. Gilbert, C.S. Becquart, C. Domain, E. Martinez, M.P. Moody, P. Bagot, D. Nguyen-Manh, D. Armstrong, Interaction of transmutation products with precipitates, dislocations and grain boundaries in neutron irradiated W, Materialia 22 (2022) 101370. https://doi.org/10.1016/j.mtla.2022.101370.
[36] M. Fukuda, K. Yabuuchi, S. Nogami, A. Hasegawa, T. Tanaka, Microstructural development of tungsten and tungsten–rhenium alloys due to neutron irradiation in HFIR, Journal of Nuclear Materials 455 (2014) 460–463. https://doi.org/10.1016/j.jnucmat.2014.08.002.
[37] J.C. He, A. Hasegawa, K. Abe, Effects of transmutation elements on the defect structure development of W irradiated by protons and neutrons, Journal of Nuclear Materials 377 (2008) 348–351. https://doi.org/10.1016/j.jnucmat.2008.03.014.
[38] T. Tanno, M. Fukuda, S. Nogami, A. Hasegawa, Microstructure Development in Neutron Irradiated Tungsten Alloys, Mater. Trans. 52 (2011) 1447–1451. https://doi.org/10.2320/matertrans.MBW201025.
[39] J. Marian, C.S. Becquart, C. Domain, S.L. Dudarev, M.R. Gilbert, R.J. Kurtz, D.R. Mason, K. Nordlund, A.E. Sand, L.L. Snead, T. Suzudo, B.D. Wirth, Recent advances in modeling and simulation of the exposure and response of tungsten to fusion energy conditions, Nucl. Fusion 57 (2017) 92008. https://doi.org/10.1088/1741-4326/aa5e8d.
[40] A. Dubinko, D. Terentyev, C. Yin, W. van Renterghem, B. Rossaert, M. Rieth, E.E. Zhurkin, A. Zinovev, C.C. Chang, S. van Dyck, G. Bonny, Microstructure and hardening induced by neutron irradiation in single crystal, ITER specification and cold rolled tungsten, International Journal of Refractory Metals and Hard Materials 98 (2021) 105522. https://doi.org/10.1016/j.ijrmhm.2021.105522.
[41] T. Suzudo, M. Yamaguchi, A. Hasegawa, Stability and mobility of rhenium and osmium in tungsten: first principles study, Modelling Simul. Mater. Sci. Eng. 22 (2014) 75006. https://doi.org/10.1088/0965-0393/22/7/075006.
[42] J.S. Wróbel, D. Nguyen-Manh, K.J. Kurzydłowski, S.L. Dudarev, A first-principles model for anomalous segregation in dilute ternary tungsten-rhenium-vacancy alloys, Journal of physics. Condensed matter an Institute of Physics journal 29 (2017) 145403. https://doi.org/10.1088/1361-648X/aa5f37.

[43] T. Suzudo, M. Yamaguchi, A. Hasegawa, Migration of rhenium and osmium interstitials in tungsten, Journal of Nuclear Materials 467 (2015) 418–423. https://doi.org/10.1016/j.jnucmat.2015.05.051.
[44] M. Fukuda, T. Tanno, S. Nogami, A. Hasegawa, Effects of Re Content and Fabrication Process on Microstructural Changes and Hardening in Neutron Irradiated Tungsten, Mater. Trans. 53 (2012) 2145–2150. https://doi.org/10.2320/matertrans.MBW201110.
[45] T. Tanno, A. Hasegawa, M. Fujiwara, J.-C. He, S. Nogami, M. Satou, T. Shishido, K. Abe, Precipitation of Solid Transmutation Elements in Irradiated Tungsten Alloys, Mater. Trans. 49 (2008) 2259–2264. https://doi.org/10.2320/matertrans.MAW200821.
[46] T. Tanno, A. Hasegawa, J.C. He, M. Fujiwara, M. Satou, S. Nogami, K. Abe, T. Shishido, Effects of transmutation elements on the microstructural evolution and electrical resistivity of neutron-irradiated tungsten, Journal of Nuclear Materials 386-388 (2009) 218–221. https://doi.org/10.1016/j.jnucmat.2008.12.091.
[47] T. Tanno, A. Hasegawa, J.-C. He, M. Fujiwara, S. Nogami, M. Satou, T. Shishido, K. Abe, Effects of Transmutation Elements on Neutron Irradiation Hardening of Tungsten, Mater. Trans. 48 (2007) 2399–2402. https://doi.org/10.2320/matertrans.MAW200722.
[48] Z.-Z. Li, Y.-H. Li, D. Terentyev, N. Castin, A. Bakaev, G. Bonny, Z. Yang, L. Liang, H.-B. Zhou, F. Gao, G.-H. Lu, Investigating the formation mechanism of void lattice in tungsten under neutron irradiation: from collision cascades to ordered nanovoids, Acta Materialia 219 (2021) 117239. https://doi.org/10.1016/j.actamat.2021.117239.
[49] L.R. Greenwood, F.A. Garner, Transmutation of Mo, Re, W, Hf, and V in various irradiation test facilities and STARFIRE, Journal of Nuclear Materials 212-215 (1994) 635–639. https://doi.org/10.1016/0022-3115(94)90136-8.